Development of chitosan base graphene oxide/ WO_3 hybrid composite for supercapacitor application

V. Thennarasu, A. Prabakaran*
Department of Physics,Vel Tech Rangarajan Dr.Sagunthala R&D Institute of Science and Technology, Avadi, Chennai-600062, Tamil Nadu, India

The use of non-renewable energy has brought to serious environmental problems for the planet. The amount of greenhouse gases rose immediately as the combustion of fossil fuels increased. As a result, sea levels are steadily rising and the Earth is becoming warmer. Research on renewable energy sources has been done extensively to provide a solution. However, in order to maximise energy utilisation, renewable energy needs an energy storage system, such as a super capacitor. For the development of sustainable supercapacitors for future energy systems, electrode material is a prospective target. The formation of desired electrode material is essential in order to fabricate supercapacitor with higher power density and longer life cycle than secondary batteries in electronic application. In this study, chitosan (CS) was isolated from crab shells, and graphene oxide (GO) was synthesized using a modified Hummers' process, followed by a chemical reduction approach. Based on the results, the synthesized GO exhibited higher capacitance as compared to GO that synthesized through single-step modified Hummers' method. Continuous efforts have been exerted to further improve the electrochemical performance of GO/WO_3 nanocomposite by incorporating an optimum content of WO_3. In this manner, comprehensive investigations on different parameters, such as loadings of ammonium paratungstate (APT), hydrothermal temperature and reaction time were conducted in order to study the formation of GO/WO_3 nanocomposite. WO_3 and GO/WO_3 nanocomposite were successfully synthesized through a simple hydrothermal method.

(Received July 27, 2023; Accepted October 19, 2023)

Keywords: Chitosan, Graphene Oxide, Composite, Supercapacitor

1. Introduction

Chitosan, the world's second most abundant biopolymer, [1], is composed of acetylglucosamine and glucosamine residues [2]. It is a valuable polymer as it can be easily obtained from marine wastes, including crustaceans and microorganisms such as fungi [3]. Chitosan can be produced in a variety of molecular weights (MW) and degrees of deacetylation (DA). Following the DA process, chitosan has been extracted from the solution in the form of powder, fibre, and sponges [4]. The solubility of chitosan has a large influence on the ionic concentration, MW, pH, acid nature, DA, and distribution of acetyl groups, as well as the main chain. Chitosan is usually dissolved in weak acids, most notably 1% of 0.1 M acetic acid [5]. Furthermore, chitosan can be dissolved in water in the presence of glycerol 2-phosphate at a neutral pH [6]. This type of chitosan is appropriate for plant-based applications [7]. A stable solution can be obtained at room temperature. On the other hand, it endorses reversible gel formation above 40 °C.In comparison to chitin, chitosan possesses better complex-forming ability, which has been attributed primarily to the existing free NH2 groups distributed along its main chain [8].A partly deacetylated chitin derivative called chitosan is a copolymer made up of units of -(14)-2-acetamido-D-glucose and -(14)-2-amino-D-glucose [9]. The R1, R2, and R3 radicals in the structure of chitosan correspond to hydrogen that is present in both the molecules of ordinary chitin and chitosan. Hydroxyl (OH) and amino (NH2) surface group production is the outcome of

* Corresponding author: draprabakaran@veltech.edu.in
https://doi.org/10.15251/JOR.2023.195.597

these surface groups. They are in charge of the chitosan organic changes that could result in polymeric derivatives of these substances [10].

Fig. 1. Schematic illustration of graphene synthetic routes from waste sources [11].

There are numerous uses for the graphene that is produced from graphite. P. R. Wallace first theorised about single-layer graphene in 1947. In 2004 [12], it was generated and recognised clearly for the first time. Several initiatives have been attempted to manufacture graphene in large quantities in a few areas, most notably chemistry and materials research [13]. Recent pricing checks indicate that authorised budgets for producing graphene and its derivatives reached $67 million in 2015 and are projected to rise to $680 million by 2020 [14]. A single layer of hexagonal graphite with sp2-hybridized carbons and sigma links makes up graphene [15]. Furthermore, delocalized π-type bonds are formed from the remaining p or σ orbitals. It has a two-dimensional structure composed of a layer of carbon atoms that are covalently connected in the form of hexagonal lattices [16]. This is the fundamental structure of many carbon allotropes [17]. Graphene possesses unique properties, such as a 1.42 Å carbon-carbon connection interval, a 3.3 Å thickness, a large surface area, high movement ability and significant optical, mechanical, electrical and thermal properties [18]. Meanwhile, GO was produced by the oxidation of graphite, which is composed of graphene and other functional groups, such as –C=O, –OH, –COOH and –COC– [19]. The existence of oxygenated functional groups on the surface of GO has caused it to have higher capacitance than graphene despite having a smaller surface area [20]. Both GO and reduced graphene oxide (rGO) have great potential to be used in energy-related applications due to their high capacitance, impressive efficiency and enhanced properties as compared to graphene [21]. A wide range of synthetic methods have been utilized to convert graphene from waste materials, which are presented in Figure 1.

Nanostructured tungsten trioxide (WO_3), as one of the n type semiconductors with a band gap of 2.8 eV, has attracted a lot of interests in photocatalysis because of its strong adsorption within the solar spectrum (≤ 500 nm), stable physicochemical properties as well as its resilience to photo corrosions[22].Under the irradiation of visible light, photo induced electrons and holes can be produced in the conduction band and valence band of WO_3, respectively. The photo generated holes can be used to drive the water-splitting reaction to produce oxygen. Generally, nanocrystalline semiconductors have poor charge mobility and thus produce very limited photocurrent[23].The poor mobility combined with inherently slow water oxidation reactions often results in the high degree of electron and hole recombination either with the defect and trap states or within grain boundaries, which diminishes the efficiency of the photocatalytic reaction significantly. This is one of the biggest obstacles hindering the development of WO_3 as a practical photocatalyst. One possible technique of improving the efficiency of electron-hole pair separation in WO_3 is to dope WO_3 with other elements or compound (Ag, C, S, P, and TiO_2)[24].

Energy, fossil fuel and environmental pollutions are strappingly related to each other. Fossil fuel was used to generate electric energy, but it raises serious environmental issue such as global warming and climate change. Although approximately 21.3 billion tonnes of carbon dioxide (CO_2) are produced yearly, however, only half of it was absorbed in nature causing global warming. To overcome this problem, energy storage devices have attracted much attention because of their advantages. Supercapacitors, known as electrochemical capacitor, emerge as an ideal energy storage device, as they provide high power density, long cycling capability and fast charge/discharge as compared to batteries [25]. Supercapacitors can be categorized into two general classes, depending on its energy storage mechanism, namely electrical double-layer capacitors (EDLCs) and pseudocapacitors. EDLCs store energy by the electrostatic accumulation of charges at the electrode-electrolyte interface instead of storing charges in the dielectric layer. On the other hand, pseudocapacitors store energy through a conventional faradaic route involving fast and reversible redox reactions between electrolyte and electroactive materials on the surface of electrodes [26]. Consecutively to bring supercapacitor to the point of marketable promptness and start high electrochemical performance of supercapacitor, substantial research on the development of electrode materials for supercapacitor application using hydrothermal technique has been developed lately. while a number of metal oxides (i.e., Fe_2O_3, SnO_2, CO_3O_4, MnO_2, NiO and WO_3) have been reported to be supercapacitor electrode for the overall reversible redox reactions between electrolyte and electroactive materials, most of them suffer from poor cycling performance[27]. Unfortunately, the overall high rate capability for high power performance is difficult to achieve due to their low electrical conductivity properties. To date, no metal oxides have been discovered that simultaneously meets all the criteria required for highly efficient supercapacitors. In effect, a suitable candidate as an electrode for supercapacitor must have three basic criteria: (i) high specific surface area for the contact of electrolyte ions, (ii) good mechanical strength to prevent safety issue such as swelling and explosion and (iii) high electrical conductivity to avoid power loss due to internal resistance [28].

2. Experimental details

2.1. Synthesis of Graphene Oxide (GO)

In accordance with protocol, the pure graphite was put right into a beaker with 300 mL of H_2SO_4. The following step involved adding KMnO4 (35 g) gradually while stirring at 35 C for 4 hours in an ice bath. After that, the mixture was diluted with 1 L of deionized water while being held at 50 C. Deionized water was added to stop the reaction, and then 100 mL of 30% H_2O_2 was added. The oxidation process was finished when the hue of the solutions quickly transitioned from dark brown to light brown. The solid product was washed with HCl to remove the metal ions, then the acid residue was rinsed away with distilled water. The resulting GO was then dried in an oven at 80C.

2.2. Synthesis of Chitosan base rGO /WO_3 nanocomposites

In this study, the chitosan-based rGO/WO_3 nanocomposites were made using a straightforward hydrothermal deacetylation method. 0.5 g of chitosan were initially dissolved in diluted acetic acid. In order to create a homogeneous suspension, 3 mg of rGO granules were dissolved in 40 mL of deionized water and ultrasonically processed for 90 min. Then, after 6 hours of continuous stirring, 0.3 g of APT was added. The pH of the solution was then brought down to 2 by the addition of HCl. At this point, the solution's colour transitioned from black to grey, showing that the APT powder was evenly spread throughout the rGO suspension. After that, the solution was transferred to an autoclave made of Teflon-lined stainless steel and kept at 180 °C for 20 hours. The precipitate was carefully filtered, rinsed with deionized water, and dried at 60 °C after cooling. The necessary Cargoes/WO_3 nanocomposites were produced under comparable experimental conditions by adjusting the loadings of APT, hydrothermal temperature, and reaction time. By following a similar process to create composites without rGO, pure W_{O3} was created.

2.3. Preparation of Electrodes

The electrochemical characteristics of GO, rGO, WO3, and CS-rGO/WO_3 nanocomposites in 1 M Na_2SO_3 neutral aqueous electrolyte were assessed using a two electrode system. The current collector was made of nickel foams, while the separator was a cellulose membrane. Normally, active materials (such as rGO, CS, WO3 or CS-rGO/WO_3 nanocomposites), acetylene black, and polytetrafluoroethylene (PTFE) were mixed in a ratio of 80:15:5 to generate a slurry, which was then pasted on nickel foams in an area of 1 1 cm^2 as shown. In two electrolytes, 1 M Na_2SO_4 and 1 M Na_2SO_3, the electrochemical performance of CS-rGO/WO_3 composites was assessed for comparison.

3. Results and Discussion

3.1. X-ray diffraction analysis (XRD)

The XRD patterns of chitosan, Tungsten trioxide (WO_3), and reduced graphene oxide (rGO) are shown in Figure 2 (a). This type of figure is essential for explaining the mechanism of rGO generation. According to the data, pristine graphite exhibited a sharp and intense diffraction peak at 2 = 26.6°, which corresponds to the (002) plane. After pre-oxidizing graphite, there is a minor change in d-spacing from 0.33 to 0.39 nm, which is determined using Equation 3.1. This could be because modest amounts of oxygen functional groups are linked to the graphene sheet. rGO has a high diffraction peak at 10.6°, which corresponds to a d-spacing of 0.83 nm along the (001) orientation, which is much greater than the d-spacing of P-G (d = 0.39 nm) (Zainy et al., 2012). As a result, the (002) P-G peak at 2 = 26.2° relocated to 10.6°, indicating that the attachment of oxygen functional groups (i.e., hydroxyl, epoxy, carbonyl, and carboxyl) increased the interlayer distance between carbon basal planes (Cao and Zhang, 2015). After chemical reduction, the peak at 10.6° vanished, and a strongrGO peak (002) with d-spacing of 0.36 nm was identified at 2 = 24.5o, showing that most of the oxygen functional groups are eliminated, resulting in a decrease in interlayer spacing (Park et al., 2011). The broad peak of rGO reflects to its structure defects and low crystallinity index (Wang et al., 2011). Figure 2 (b) shows the XRD patterns of graphite, GO and rGO. It clearly shows that without the pre-oxidization stage, the peak due to graphite is still observed in GO, indicating the GO are not fully oxidized under same experimental conditions. The diffraction peak of rGO located at 2θ = 24.1° is very close to the diffraction peak of graphite, implying the successful reduction of rGO. As well known, graphite is formed by stacking few layers of graphene sheets together through van der Waals force.

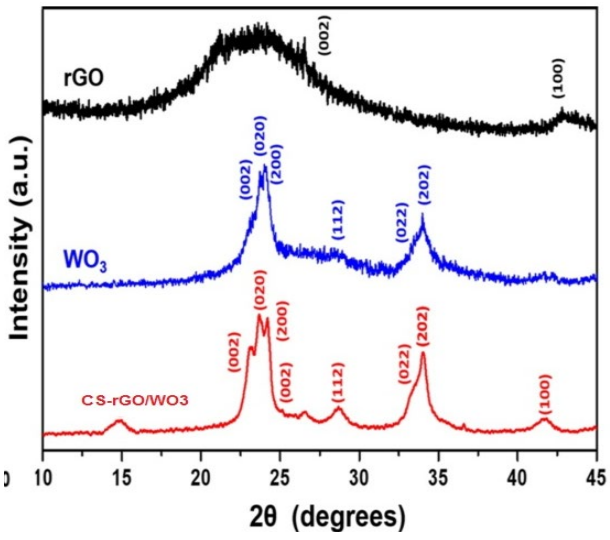

Fig. 2. XRD pattern of (a) rGO, (b) WO_3 and (c) CS-rGO/WO_3 nanocomposites.

3.2. Raman spectroscopy

Raman spectroscopy was used to further validate the decreased state of GO to rGO. The Raman spectra of rGO in Figure 3 (a) has two noticeable peaks, the D band and the G band, which were visible at 1350 cm1 and 1596 cm1, respectively. The D and G bands of GO occurred at 1355 and 1603 c^{m-1}, respectively, as can also be seen from the spectrum. In contrast, as shown in Figure 2 (b), the D band and G band of rGO were centred at 1352 and 1600 cm^{-1}, respectively. According to Bak et al. (2011), these distinctive peaks are caused by carbon atom defects and the scattering of the E2g phonon from sp^2 carbon atoms. GO and rGO both have ID/IG ratios of 0.74 and 0.84, respectively. While GO and rGO have ID/IG values of 0.85 and 0.88, respectively. Due to a disorder that develops when the oxygen groups are removed and a significant quantity of sp2 carbon networks with small average sizes are added, CS-rGO/WO_3 and rGO has the highest ID/IG ratio when compared to P-GO and GO (Chen et al., 2011). However, the ID/IG ratio of rGO is slightly lower than rGO, suggesting that the 10 20 30 40 50 60 70 80 90 002 002 001 002 rGO GO P-G 2Theta (degree) Graphite 10 20 30 40 50 60 70 80 90 rGO GO Graphite 002 001 002 2-Theta (degree) 0.0 0.5 1.0 1.5 2.0 2.5 3.0 3.5 4.0 4.5 5.0 (b) (a)Intensity (a.u.) Intensity (a.u.) rGO has larger sp^2 domains size than that of rGO. This large sp^2 domain structures result in an increased of conductivity and thus benefits the diffusion of ions (Stankovich et al., 2007). In Raman spectroscopy, the 2D band is crucial for determining how many layers of graphene sheets there are. The 2D band of single-layer graphene is commonly located at roughly 2679 cm^{-1}, according to a 2015 paper by Akhavan, but the 2D band of multi-layer graphene is blue-shifted into higher wavenumbers and is 2698 cm-1. The 2D bands of rGO and rGO were measured in this study, and the 2D bands of both molecules were found to be few-layer graphene sheets at 2689 cm1 and 2680 cm1, respectively.

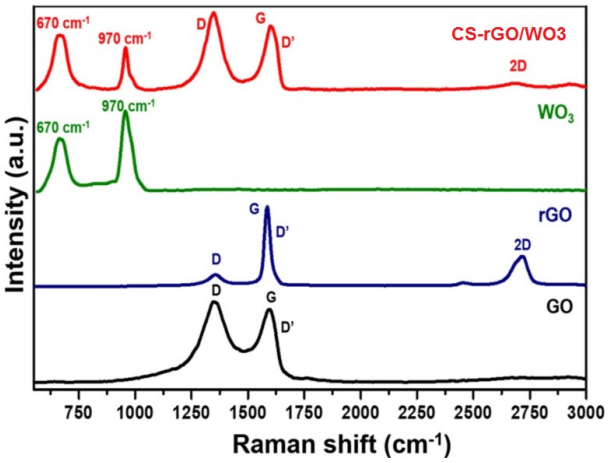

Fig. 3. Raman spectra of (a) rGO, (b) WO_3 and (c) CS-rGO/WO_3 nanocomposites.

3.3. Surface morphology analysis

The FESEM images of the synthesised CS-rGO/WO_3 nanocomposites with various APT loadings are shown in Figure 4 (a-b). It is obvious that the loading amount of APT had a significant impact on the morphologies of the GO/WO_3 nanocomposites. It was discovered that the morphologies of samples created with lower concentrations of APT (in the range of 50–100) were identical, with the fiber-like structure dispersed at random across the rGO sheets.

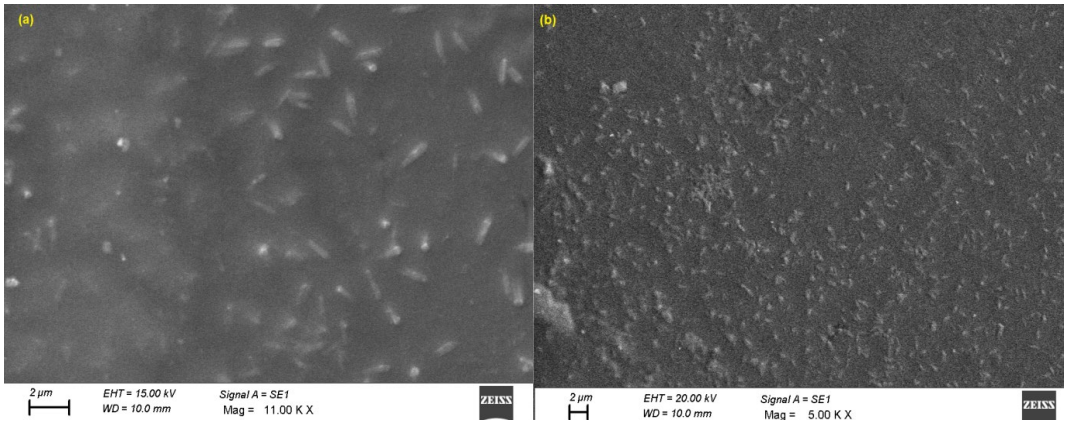

Fig. 4. Surface morphology of (a) GO/WO_3 and (b) CS-rGO/WO_3 nanocomposites.

3.4. Capacitance studies

The CV curves of the CS-rGO/WO_3 nanocomposite with various APT loading levels are shown in Figure 5(a). The CS-rGO/WO_3 nanocomposite's CV curves had almost rectangular-like forms and small redox peaks. According to Peng et al. (2014), this indicated that the CS-rGO/WO3 samples showed the synergistic effects of double-layer capacitance and pseudocapacitance, and Wang et al. (2014)a found that the reversible reactions of W6+ to W5+ and W5+ to W4+ were well represented by the two pairs of cathodic and anodic peaks**.** These results were consistent with those of the aforementioned Raman studies (Figure 5(b)), in which tungsten metal was found to have a variety of oxidation states, including W6+, W5+, and W4+, as a result of ion reduction by intercalation into a solid electrode using faradaic oxidation/reduction reactions. Additionally, Figure 5 (b) shows that the specific capacitances of 1:100, 1:150, and 1:1200 CS-rGO/WO_3 nanocomposites were determined to be 60.6, 97.6, 41.4, and 10.3 F g-1, respectively. The agglomeration of WO_3 was mostly blamed for the decrease in the specific capacitance of CS-rGO/WO_3 nanocomposites as the APT loading was increased. This is associated with the fact that agglomeration resulted in the decrease of surface area and eventually lowered the energy storage (Song et al., 2016).

As shown in Figure 5 (a), a symmetric shape of CV loop with a pair of redox peaks was recorded. This suggested the pseudocapacitive charge/discharge characteristics during the reversible intercalation/de-intercalation of ions leading to an additional capacitance. Figure 5 (b) shows the specific capacitance values of the CS-rGO/WO3 nanocomposites calculated from the discharge curves. The specific capacitances for samples synthesized at 120, 150, and 180 ºC were determined to be 20.9, 274.0 and 97.6 F g^{-1} , respectively. It is worth to mention that the significant improved electrochemical performance of the sample synthesized at 150ºC may be ascribed to the thin fiber-like WO3 acting as the spacer to inhibit the agglomeration of CS-rGO (An et al., 2012), which could subsequently increase the surface area for the electrolyte access and promote the mobility of ions. Apart from that, it was found that the sample prepared at 120 ºC exhibited the lowest specific capacitance because of 120 ºC might be insufficient to get rid of the potential energy barrier to form fiber-like WO3. At 180 ºC, the low specific capacitance was presumably dominated by the agglomeration of fiberlike WO3. Additionally, the sample prepared at 150 ºC (6.92 Ω) exhibited a semicircle smaller than that of those 120 and 180 ºC (Figure 5 (c)). The smaller diameter of semicircle (Rct) might be attributed to the direct WO3 grown on P-rGO allowing higher diffusion of electrolyte ion at electrode interface (Rakhi et al., 2016). In comparison with 120 and 180 ºC, the straight line slope of the sample prepared at 150 ºC was greater than that of 45º, revealing a superior capacitive behavior with low diffusion resistance (inset Figure 5 (c)). It is also clearly shown in Figure 5 (d) that the composite synthesized at 150 ºC possessed a relatively lower diffusive resistance considering only the single peak (ϕ2) was observed at high frequency region. This is ascribed to the fact that the introduction of 1D h-WO3 into CS-rGO could prevent the agglomeration of CS-rGO and reduce the path length for ions diffusion.

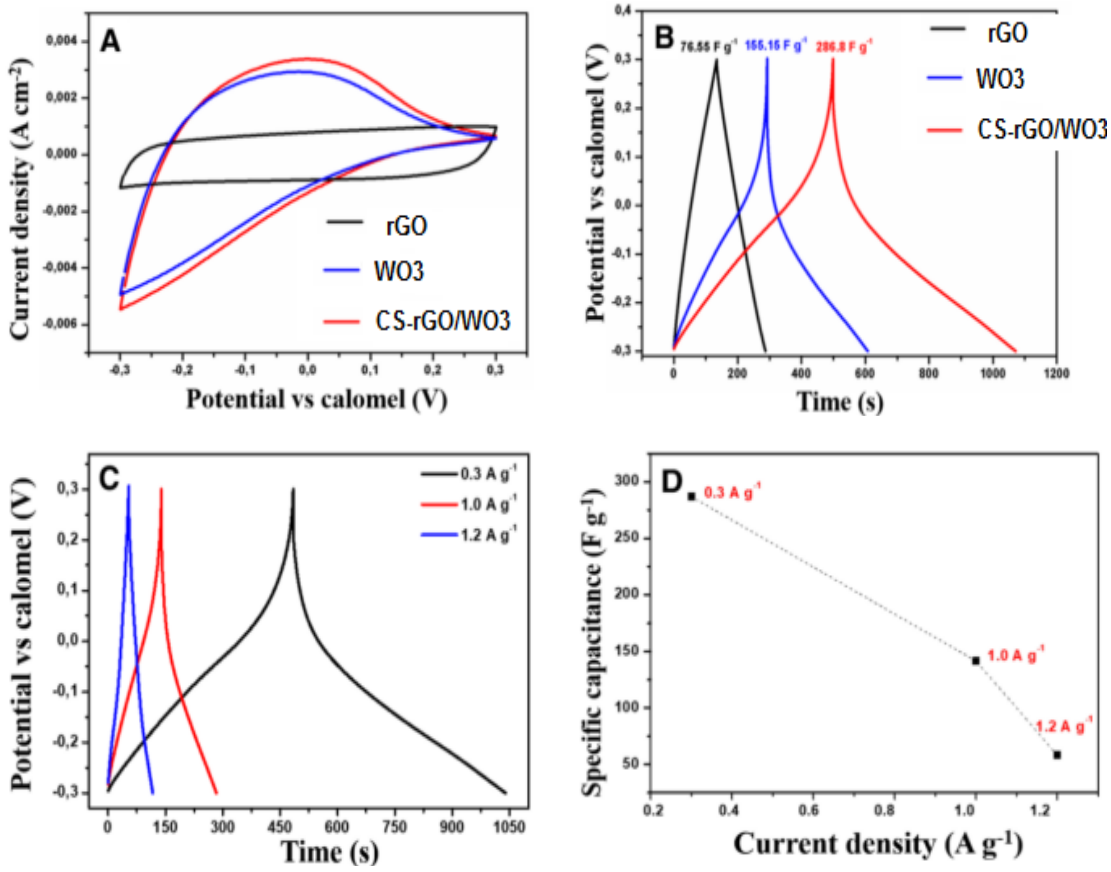

Fig. 5. Electrochemical performance of rGO, WO3 and CS-rGO/WO_3. (a) Cyclic voltammogram measured at scan rate of 25 mV s^{-1}; (b) Galvanostatic charge/discharge curves measured at current density of 0.7 A g^{-1} ; and (c) Nyquist plot of rGO and CS-rG/WO_3. The inset shows the enlarged high frequency region.

3.5. Electrochemical Impedance spectroscopy

Based on aforementioned discussion, equivalent series resistance (ESR) is inverse proportional to the capacitive behavior. Hence, electrochemical impedance spectroscopy (EIS) measurement was conducted to study the electrical conductivity of electrode. Nyquist plot shows that ESR is obtained from the intercept at the real axis (Z') of Nyquist plot in high frequency region, semicircle in medium frequency region and straight line in low frequency region is related to diffusive resistance or Warburg impedance ([28]. ESR composed a series of resistance including electrolyte resistance, internal resistance of the substrate and contact resistance between current collector and material. The inset in Figure 6 (a) demonstrated that the ESR values of GO and CS-rGO/WO3 are 0.91, and 1.22 Ω, respectively. Changing in ESR value can be accredited to the different conductance value of and rGO. Typically, the lower the ESR value is, the higher the conductivity of an electrode material will be. Moreover, rGO electrode also exhibited the smallest diameter of semicircle in comparison with GO and rGO, indicating CS-rGO/WO3 possesses lower charge transfer resistance (Rct) as shown in inset of Figure 6(a). According to fitted results, the Rct value decreases according to the following order: GO (9.59 Ω) > rGO (5.24 Ω) > P-GO (3.17 Ω) > P-rGO (2.05 Ω). As shown in Figure 6 (b), all electrodes appear to have a vertical straight line nearly parallel to imaginary (Z") axis at low frequency, resulting in low ion diffusion resistance in the electrode. However, the curve of GO was slight bend, suggesting high ion diffusion resistance within electrode.

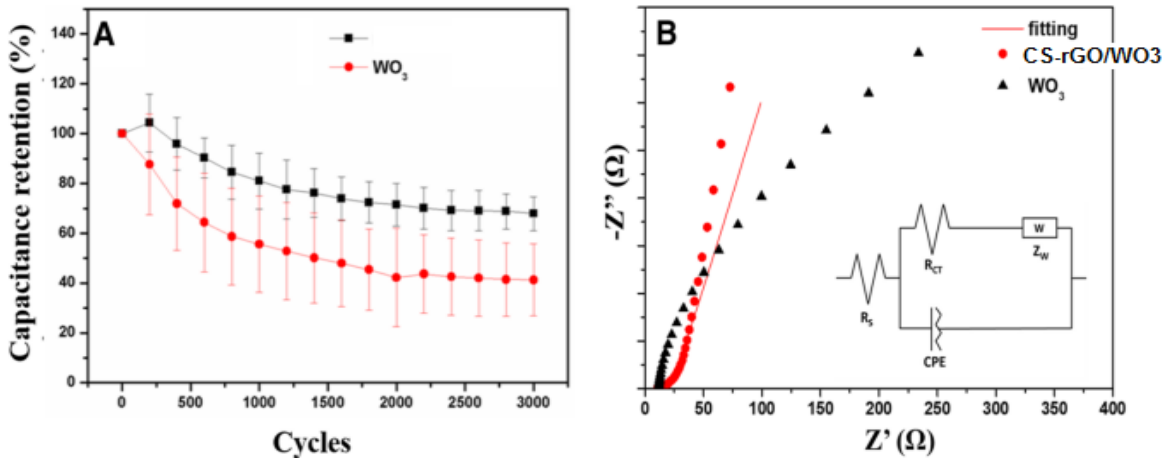

Fig. 6. (a) Nyquist plot of CS-rGO/WO_3 nanocomposite and (b) WO_3 at open circuit potential (OCP) (the inset of enlarged high frequency region).

4. Conclusion

In summary, the process for synthesis of CS, WO_3, and rGO was determined. The following were the findings from this section of the research: (i) The two-step modified Hummers' approach was used to successfully synthesise r-GO. When r-GO was compared to GO synthesised using a single-step modified Hummers' method, it had greater interlayer spacing and more oxygen functional groups attached. This high interlayer spacing facilitates the restoration of the sp2 structure during the chemical reduction process, resulting in a high electrolyte ion diffusion rate; (ii) CS, WO_3, and rGO were effectively synthesised utilising the chemical reduction approach. The conductivity of CS, rGO, and WO_3 nanocomposites was increased as a result of this restoration. The rGO obtained was then used to create a CS-rGO/WO_3 nanocomposite.

Interestingly, rGO/WO_3 nanocomposite with mass ratio of 1:100 showed the highest specific capacitance of 274 F g-1 under optimal conditions of 150 ºC and 20 h, give rise to 2-fold increment of specific capacitance over pure WO_3. A working voltage range of -0.8 to 0.8 V and high energy density of 121 Wh kg-1 at power density of 780.4 W kg-1 were obtained for rGO/WO_3 based symmetric cell. More significantly,CS-rGO/WO_3 nanocomposite exhibited a good cycling performance and retained 75% of initial capacitance after 1000 cycles of galvanostatic charge/discharge. By carefully control the synthesis parameters (i.e., loadings of APT, temperature and reaction time), fiber-like structure of CS-rGO/WO_3 nanocomposite was obtained and exhibited lower resistance due to fiber-like WO_3 acting as the spacer to prevent the restacking of rGO as well as to provide a larger surface area for electrolyte access. Moreover, the addition of conductive rGO could decrease the resistance of ions between the electrolyte and electrode, leading to fast electron transport. A possible formation of WO_3 on rGO and WO_3 as an effective synergist is proposed. The present experimental works provide a better understanding on the role of fiber-like WO3 in anchoring rGO/WO_3 nanocomposite for efficient electrochemical study.

References

[1] Wang, W.; Meng, Q.; Li, Q.; Liu, J.; Zhou, M.; Jin, Z.; Zhao, K., Int. J. Mol. Sci. 2020, 21, 487; https://doi.org/10.3390/ijms21020487

[2] Kumar, M.R.; Muzzarelli, R.; Muzzarelli, C.; Sashiwa, H.; Domb, A.J., Chem. Rev. 2004, 104, 6017-6084; https://doi.org/10.1021/cr030441b

[3] Shariatinia, Z., Adv. Colloid Interface Sci. 2019, 263,131-194; https://doi.org/10.1016/j.cis.2018.11.008

[4] Sahariah, P.; Masson, M., Biomacromolecules 2017, 18, 3846-3868; https://doi.org/10.1021/acs.biomac.7b01058

[5] Cheung, R.C.F.; Ng, T.B.; Wong, J.H.; Chan, W.Y., Mar. Drugs 2015, 13, 5156-5186; https://doi.org/10.3390/md13085156

[6] Choi, C.; Nam, J.P.; Nah, J.W., J. Ind. Eng. Chem. 2016, 33, 1-10; https://doi.org/10.1016/j.jiec.2015.10.028

[7] Zhang, L.; Zeng, Y.; Cheng, Z., J. Mol. Liq. 2016, 214, 175-191; https://doi.org/10.1016/j.molliq.2015.12.013

[8] Cavallaro, G.; Micciulla, S.; Chiappisi, L.; Lazzara, G., J. Mater. Chem. B 2021, 9, 594-611; https://doi.org/10.1039/D0TB01865A

[9] Karimi-Maleh, H.; Ayati, A.; Davoodi, R.; Tanhaei, B.; Karimi, F.; Malekmohammadi, S.; Orooji, Y.; Fu, L.; Sillanpää, M., J. Clean. Prod. 2021, 125,880; https://doi.org/10.1016/j.jclepro.2021.125880

[10] Si, Z.; Hou, Z.; Vikhe, Y.S.; Thappeta, K.R.V.; Marimuthu, K.; De, P.P.; Ng, O.T.; Li, P.; Zhu, Y.; Pethe, K.; et al., ACS Appl. Mater. Interfaces 2021, 13, 3237-3245; https://doi.org/10.1021/acsami.0c20881

[11] Brasselet, C.; Pierre, G.; Dubessay, P.; Dols-Lafargue, M.; Coulon, J.; Maupeu, J.; Vallet-Courbin, A.; de Baynast, H.; Doco, T.; Michaud, P.; et al., Appl. Sci. 2019, 9, 1321; https://doi.org/10.3390/app9071321

[12] Ikram, R.; Jan, B.M.; Ahmad, W., J. Mater. Res. Technol. 2020, 9, 11587-11610; https://doi.org/10.1016/j.jmrt.2020.08.050

[13] Ikram, R.; Jan, B.M.; Ahmad, W., J. Mater. Res. Technol. 2020, 9, 15924-15951; https://doi.org/10.1016/j.jmrt.2020.11.043

[14] Azizi-Lalabadi, M.; Jafari, S.M., Adv. Colloid Interface Sci. 2021, 292, 102416; https://doi.org/10.1016/j.cis.2021.102416

[15] Tiwari, S.K.; Sahoo, S.; Wang, N.; Huczko, A., J. Sci. Adv. Mater. Devices 2020, 5, 10-29; https://doi.org/10.1016/j.jsamd.2020.01.006

[16] Olabi, A.G.; Abdelkareem, M.A.; Wilberforce, T.; Sayed, E.T., Renew. Sustain. Energy Rev. 2021, 135, 110026; https://doi.org/10.1016/j.rser.2020.110026

[17] Balandin, A.A., ACS Nano 2020, 14, 5170-5178; https://doi.org/10.1021/acsnano.0c02718

[18] Tarcan, R.; Todor-Boer, O.; Petrovai, I.; Leordean, C.; Astilean, S.; Botiz, I., J. Mater. Chem. C 2020, 8, 1198-1224; https://doi.org/10.1039/C9TC04916A

[19] Ahmad, W.; Ur Rahman, A.; Ahmad, I.; Yaseen, M.; Mohamed Jan, B.; Stylianakis, M.M.; Kenanakis, G.; Ikram, R., Nanomaterials 2021, 11, 203; https://doi.org/10.3390/nano11010203

[20] Ikram, R.; Mohamed Jan, B.; Vejpravova, J.; Choudhary, M.I.; Zaman Chowdhury, Z. Nanomaterials 2020, 10, 2004; https://doi.org/10.3390/nano10102004

[21] Sun, Z.; Fang, S.; Hu, Y.H., Chem. Rev. 2020, 120, 10336-10453; https://doi.org/10.1021/acs.chemrev.0c00083

[22] Zhao ZG, Miyauchi M., Angew Chem Int Ed, 2008, 47: 7051-7055; https://doi.org/10.1002/anie.200802207

[23] L. Zhao, X. F. Chen, X. C. Wang, Y. J. Zhang, W. Wei, Y. H. Sun, M. Antonietti and M. M. Titirici, Adv. Mater., 2010, 22, 3317-3321; https://doi.org/10.1002/adma.201000660

[24] B. W. Mwakikunga, A. Forbes, E. Sideras-Haddad, M. Scriba, E. Manikandan, Self Nanoscale Res. Lett., 2010, 5, 389-397; https://doi.org/10.1007/s11671-009-9494-4

[25] Huang, H., Yue, Z., Li, G., Wang, X., Huang, J., Du, Y., Yang, P. (2013a). Journal of Materials Chemistry A, 1(47): 15110-15116; https://doi.org/10.1039/c3ta13433d

[26] Faraji, S., and Ani, F. N. (2014), Journal of Power Sources, 263: 338-360; https://doi.org/10.1016/j.jpowsour.2014.03.144

[27] Bonso, J. S., Rahy, A., Perera, S. D., Nour, N., Seitz, O., Chabal, Y. J., Balkus, K. J., Ferraris, J. P., Yang, D. J. (2012), Journal of Power Sources, 203: 227-232;

https://doi.org/10.1016/j.jpowsour.2011.09.084
[28] Davies, A., and Yu, A. (2011), The Canadian Journal of Chemical Engineering, 89(6): 1342-1357; https://doi.org/10.1002/cjce.20586